# Navier-Stokes Computations for Circulation Control Airfoils

THOMAS H. PULLIAM,
DENNIS C. JESPERSEN,
AND
TIMOTHY J. BARTH

Research Scientists
Computational Fluid Dynamics Branch
NASA Ames Research Center

**Abstract.** Navier-Stokes computations of subsonic to transonic flow past airfoils with augmented lift due to rearward jet blowing over a curved trailing edge are presented. The approach uses an innovative spiral grid topology. Solutions are obtained using a Navier-Stokes code (ARC2D) which employs an implicit finite difference method, an algebraic turbulence model, and some recent developments which improve stability, convergence and accuracy. Results are compared against experiments for no jet blowing and moderate jet pressures and demonstrate the unique capability to compute these complicated flows.

## I. INTRODUCTION

This paper presents details of an effort to compute the flow around an airfoil with augmented lift caused by an exhausting rearward jet over a curved trailing edge (Coanda effect). Abramson and Rogers[1] give a good discussion of the circulation control airfoil problem and Coanda effect. A recent review paper by Wood and Nielsen[2] also describes the physical problem and experimental methods. The computations performed here combine a well established flow solver for the thin-layer Navier-Stokes equations (ARC2D)[3] with a number of new concepts for grid generation and integration. A spiral grid topology is used to provide adequate resolution inside the jet plenum chamber, around the Coanda surface and then out to the far field boundary. By manipulating the data base an integration scheme for this topology is employed which does not create any nonphysical boundaries.

The computations are compared with experimental data for cases with and without jet blowing. Results show good agreement with experimental data with significant lift augmentation for the blowing cases. Lift augmentation (defined as the lift to blowing rate curve slope) is compared with experimental data for various Mach numbers, angles of attack, and two Coanda geometries. The data of Abramson and Rogers[1] provides a useful set of experimental results for comparison.

This computational effort provides a needed tool for examining these complicated flows, especially in the jet exit-Coanda surface region where experimental measurements are difficult to obtain. The purpose of this paper is to demonstrate the application of ARC2D to a very interesting physical problem. We are interested in demonstrating the capibility to compute relevant trends from the experimental data. Once a validation of the present method is accepted, we then hope to use these computational experiments to aid in our understanding of the physical mechanisms inherent in the circulation control problem.

## II. SPIRAL GRID GENERATION

One goal of this effort was to compute rather than model the flow at the jet exit. To do this we require a grid extending into the plenum. In order to easily utilize the existing Navier-Stokes solver ARC2D, a mapping from physical space to a computational rectangle was desired. These considerations led us to design a spiral grid mapping. The grid "begins" in the chamber, continues out the plenum exit, and wraps around the airfoil several times, spiraling away from the airfoil as it wraps around. Figure 1 shows the correspondence between physical and computational space.

In implementing this procedure, we use an intermediate step employing the mapping $z = \cos(\zeta)$ from the complex $\zeta$-plane to the complex $z$-plane. This function is $2\pi$-periodic in $\zeta$, takes horizontal lines in the $\zeta$-plane to ellipses in the $z$-plane, takes vertical lines in the $\zeta$-plane to hyperbolas in the $z$-plane, and takes lines with positive slope in the $\zeta$-plane to outward-spiraling curves in the $z$-plane. We are given coordinates for the airfoil shape in physical space, defining a curve $C_z$ running clockwise from a point on the Coanda surface beneath the jet exit around to the last point on the lip above the slot. Using the one-dimensional distribution function of Vinokur[4], we locate a given number of points around the airfoil with prescribed arclength spacings in the Coanda region and at the leading edge. (Sometimes the function from Vinokur[4] stretches too slowly, in which case we use a simple polynomial distribution function.) In a typical case we might have 281 points around the airfoil, with 120 of those points aft of 95% chord to give adequate circumferential resolution in the Coanda region. We then find the prei-mages $\zeta_j$ of these points $z_j$, i.e., $\cos(\zeta_j) = z_j = x_j + iy_j$. These points $\zeta_j = \alpha_j + i\beta_j$ are found by a simple Newton iteration and define a curve $C_\zeta$ in the $\zeta$-plane. This curve is of the form $\beta = \beta(\alpha)$, $\alpha_{min} \leq \alpha \leq \alpha_{jet}$. We then extend this curve for $\alpha_{jet} \leq \alpha \leq \alpha_{max}$, where $\alpha_{max}$ is chosen so that the grid spirals around the airfoil a prescribed number of times (usually about 3.5) in physical space. Thus we have a curve $\beta = \beta_{bottom}(\alpha)$, $\alpha_{min} \leq \alpha \leq \alpha_{max}$, in the $\zeta$-plane.

We then define the upper boundary of the region in the $\zeta$-plane via $\beta = \beta_{top}(\alpha) = \beta_{bottom}(\alpha + 2\pi)$, and we also ensure that $\beta_{top}$ is defined for $\alpha_{min} \leq \alpha \leq \alpha_{max}$. This results in a distorted rectangle in the $\zeta$-plane, $\{(\alpha, \beta) : \alpha_{min} \leq \alpha \leq \alpha_{max}, \quad \beta_{bottom}(\alpha) \leq \beta \leq \beta_{top}(\alpha)\}$. We make a grid on this region as follows. The points $\alpha_j$ are defined by periodicity. A given number of points (typically 31) are distributed in the $\beta$-direction,

with the normal spacing in the $\varsigma$-plane chosen to result in a prescribed normal spacing (typically 0.002% of chord) at the airfoil surface in the physical plane. The one-dimensional stretching function is used for the distribution in the $\beta$-direction. Care is also taken that the grid spacing in physical space is continuous as wrap boundaries are crossed moving away from the airfoil. Finally, a few (typically 10) Jacobi relaxation steps are taken, again working in $\varsigma$-space, to enhance the smoothness of the grid.

The grid in the chamber is made in a separate step, working entirely in physical space. Continuity of grid spacing in the circumferential direction is enforced at the jet exit. Typically we use 71 grid points in the flow direction for the grid in the chamber. The last step is to transform the grid in the $\varsigma$-plane to the $z$-plane via the cosine mapping and "weld" on the grid in the chamber. The total process is algebraic and explicit and results in a grid which extends into the plenum and gives good resolution in the Coanda region. The dimensions of the final grid are typically $1065 \times 31$. The mapping $z = \cos(\varsigma)$ is conformal but the grid in physical space is not orthogonal since the grid in $\varsigma$-space is not orthogonal.

Abramson and Rogers[2] tested three different Coanda geometries for one basic elliptical slightly cambered airfoil. We have chosen two of the geometries, the rounded ellipse (RE) and the displaced ellipse (DE). The forebody for both cases is identical and a replaceable Coanda geometry was employed. Figure 2 shows the differences in shape and curvature between the RE and DE geometries. These may seem small, but experimental evidence shows a large effect of Coanda geometry on lift augmentation and response to various flow parameters such as Mach number and angle of attack. Plate 1 shows various views of the grid used for the RE computations. Note the continuity across wrap boundaries, the chamber–Coanda region and the clustering in the Coanda base region. The DE grid is similar. Both grids are $1065 \times 31$ with 281 points on the airfoil.

## III. NAVIER-STOKES SOLVER

The Navier-Stokes solver (ARC2D)[3] used for the computations was written at NASA Ames Research Center. The thin-layer Navier-Stokes equations in generalized coordinates are solved using an implicit approximate factorization technique. This code is explained in detail in papers by Pulliam[3], Steger[5] and Pulliam and Steger[6] and will not be reviewed at length here. The main features of this code are presented below. The thin-layer Navier-Stokes equations written in generalized curvilinear coordinates are

$$\partial_\tau \hat{Q} + \partial_\xi \hat{E} + \partial_\eta \hat{F} = Re^{-1} \partial_\eta \hat{S} \tag{1}$$

where

$$\widehat{Q} = J^{-1}\begin{bmatrix}\rho\\ \rho u\\ \rho v\\ e\end{bmatrix}, \quad \widehat{E} = J^{-1}\begin{bmatrix}\rho U\\ \rho uU + \xi_x p\\ \rho vU + \xi_y p\\ U(e+p) - \xi_t p\end{bmatrix},$$

$$\widehat{F} = J^{-1}\begin{bmatrix}\rho V\\ \rho uV + \eta_x p\\ \rho vV + \eta_y p\\ V(e+p) - \eta_t p\end{bmatrix}$$

$$\widehat{S} = J^{-1}\begin{bmatrix}0\\ \eta_x m_1 + \eta_y m_2\\ \eta_x m_2 + \eta_y m_3\\ \eta_x(um_1 + vm_2 + m_4) + \eta_y(um_2 + vm_3 + m_5)\end{bmatrix}$$

with

$$U = \xi_t + \xi_x u + \xi_y v, \quad V = \eta_t + \eta_x u + \eta_y v$$

$$m_1 = \mu(4\eta_x u_\eta - 2\eta_y v_\eta)/3$$
$$m_2 = \mu(\eta_y u_\eta + \eta_x v_\eta)$$
$$m_3 = \mu(-2\eta_x u_\eta + 4\eta_y v_\eta)/3$$
$$m_4 = \mu Pr^{-1}(\gamma - 1)^{-1}\eta_x \partial_\eta(a^2)$$
$$m_5 = \mu Pr^{-1}(\gamma - 1)^{-1}\eta_y \partial_\eta(a^2)$$

These equations are central space differenced and implicitly advanced in time. For $h = \frac{1}{2}$ or 1. the time integration is trapezoidal rule (second order in time) or Euler implicit (first order in time)

$$\left[I + h\partial_\xi \widehat{A}^n\right]\left[I + h\partial_\eta \widehat{B}^n - Re^{-1}hJ^{-1}\partial_\eta \widehat{M}\right]\Delta\widehat{Q}^n = -h\left(\partial_\xi \widehat{E}^n + \partial_\eta \widehat{F}^n - Re^{-1}\partial_\eta \widehat{S}^n\right) = \widehat{R}^n \tag{2}$$

where $\widehat{A}, \widehat{B}$, and $\widehat{M}$ are Jacobians of $\widehat{E}, \widehat{F}$, and $\widehat{S}$ respectively.

An explicit nonlinear artificial dissipation term is added to enhance stability of the central difference scheme. The form, a mixture of constant coefficient fourth order and variable coefficient second order terms, has proven to be very successful in obtaining accurate results for subsonic and transonic calculations. Details can be found in References [3], [6] and [7].

For steady-state computations or first order time integrations, a diagonal form of Eq. (2) is used. In this case the left and right eigenvector matrices of $\widehat{A}$ and $\widehat{B}$ are

used to diagonalize the one-dimensional operators. Pulliam[3,8] gives a discussion and derivation of this algorithm. The diagonal algorithm can be written as

$$T_\xi \left[I + h\,\delta_\xi \Lambda_\xi\right] \hat{N} \left[I + h\,\delta_\eta \Lambda_\eta\right] T_\eta^{-1} \Delta \hat{Q}^n = \hat{R}^n \tag{3}$$

where

$$\Lambda_\xi = T_\xi^{-1} \hat{A} T_\xi \quad \text{and} \quad \Lambda_\eta = T_\eta^{-1} \hat{B} T_\eta$$

with $T_\xi$ the matrix whose columns are the eigenvectors of $\hat{A}$ and $T_\eta$ the corresponding eigenvector matrix for $\hat{B}$ and $\hat{N} = T_\xi^{-1} T_\eta$. The main advantage of this form is the simplification of the matrix inversions from block inversions to scalar inversions. This reduces the computational work and makes it easier to vectorize the implicit scheme. Also, the new scalar form for the inversion process allows for the use of scalar pentadiagonal solvers so that the added fourth order explicit artificial dissipation can be properly linearized and made fully implicit. This enhances stability and convergence rates ( Refs. [3] and [6].) In viscous calculations the diagonal algorithm employs an approximation to the implicit viscous terms where the eigenvalues of the viscous Jacobian, are added to the inviscid eigenvalues for the $\eta$ derivatives on the left-hand side of Eq. (3), Ref. [3]

## IV. BOUNDARY CONDITIONS

The boundary conditions used at the airfoil surface and far field boundary are standard ones defined in Refs. [3] and [6]. Briefly, no slip is enforced at the surface along the plenum walls and airfoil surface. The normal pressure gradient is set to zero at the solid surfaces and an adiabatic temperature boundary condition is used. Characteristic conditions based on local one-dimensional Riemann invariants are used at the far field boundary. A correction based on a potential vortex at the airfoil center with a circulation consistent with the generated lift is also used to reduce the effect of the location of the outer boundary.

At the plenum inlet, conditions are specified so that a required mass flow rate is obtained at the slot exit. The geometry used in the plenum was supplied by Abramson and Rogers[1] along with an estimated slot height. For a pressure ratio $P_r$ and temperature ratio $T_r$ (plenum values to free stream values) mass flow rates were measured by Abramson and Rogers. A nondimensional mass flow parameter, $C_\mu$ is defined as

$$C_\mu = \frac{\dot{m} V_j}{\frac{1}{2} M_\infty} \tag{4}$$

where $\dot{m}$ is mass flow rate, $M_\infty$ is free stream Mach number and

$$V_j = \sqrt{2 T_r \frac{\gamma}{\gamma - 1} \left[1 - P_r^{-(\gamma - 1/\gamma)}\right]} \tag{5}$$

is an isentropic jet velocity. Experimentally, some expansion of the slot can occur when the plenum is pressurized, which will then alter the mass flow rates. The slot heights given by Abramson and Rogers were estimated from an isentropic relation and were on the order of 0.0021 (based on a chord of 1.0) for the geometries considered. In order to match mass flow rates computationally, since the computational geometry is rigid, the slot heights for the RE and DE were modified slightly. We employed a value of 0.0025 for both cases which enabled us to match mass flow rates to within 3%. Figure 3 shows a correlation between the experimental mass flow rates and the computed values for the cases presented below. An exact correlation would be along the 45 degree line and we see quite acceptable results.

## V. SPIRAL INTEGRATION

The grid generation procedure maps the flow region in physical space to a rectangular box in computational space (Fig. 1). The use of the spiral grid topology requires us to reexamine our usual integration procedures. The $\xi$ integration of Eq. (3) is a straightforward integration from the plenum chamber boundary (a-b) to the farfield boundary (c-d). In the $\eta$ direction, a first glance at the topology in computational space shows that spiral boundaries occur as interior boundaries in physical space. These are not physical boundaries but rather constructs of the grid generation. A continuous integration across these boundaries is obtained by reordering the computational domain. Plate 1 shows views of the spiral grid where the plenum is shown in red and sequential wraps of the grid are shown in different colors.

The implicit integration scheme, Eq. (3), can be rewritten symbolically as

$$L_\eta L_\xi \Delta \hat{Q}^n = (R_\xi + R_\eta)\, \hat{Q}^n \tag{6}$$

where $L$ represents an implicit operator and $R$ an explicit operator. The first step in the integration is to perform the explicit $R_\xi$ differencing using the data in what will be called the $\xi$ orientation, Fig. 1. The computational domain is then reordered by an in-place transpose to the $\eta$ orientation. The reordered computational domain is shown in Fig. 4, and in Plate 2 the distinct $\eta$ blocks are painted different colors. Here the blocks of data constituting a spiral wrap are stacked on top of each other. In this new computational space we integrate in $\eta$ from wall to wall in the plenum region and from the body surface to the far field boundary in the outer region. Both the explicit $R_\eta$ and implicit $L_\eta$ operations are performed at this time. Note that if the last wrap is not a full wrap then we actually define three regions and integrate from boundary to boundary for each. After the $\eta$ integration is complete the data is reordered to the $\xi$ orientation and the implicit $L_\xi$ integration is performed, completing the algorithm. Using this integration technique, we only encounter boundaries which are physically meaningfull (on the airfoil surface, at the plenum chamber inflow and at the far field boundary). The spiral wrap boundaries that physically lie in the interior of the domain of integration are treated at regular interior ponits and are solve using

the conservation equations. That is, they are treated no differently than any other interior point.

## VI. TURBULENCE MODEL

There are a number of interesting physical mechanisms associated with the circulation control problem. In the absence of the exhausting rearward jet, the blunt body geometry produces base flow separation and the expected $C_l - \alpha$ responses. High positive and negative angles of attack produce viscous stall and at low angles of attack there is very little lift and substantial drag. As the pressure in the chamber increases a jet exhausts out the slot and remains attached to the Coanda surface. The flow off the upper airfoil surface is entrained at the jet–shear layer–upper boundary layer interface. This entrainment of the upper surface flow produces the augmented lift via increased circulation. As the blowing rate is increased the airfoil continues to gain lift until a stall boundary is reached. The nature and cause of this stall is not fully understood. It has been characterized as an "inviscid stall" as opposed to the classical viscous airfoil stall. Although the authors are quite interested in this stall mechanism, such cases are beyond the capabilities of the current turbulence model used here and also require more study into the basic physical mechanisms involved in the prestall conditions. Computations attempted at the post-stall conditions were unsteady and not quite acceptable.

One of the more important effects needed in this problem is the jet–upper boundary layer interaction. The boundary layer generated on the upper surface will be strongly dependent on the upper surface geometry, the flow conditions (such as freestream Mach number or angle of attack), and the increased accelerations due to the jet entrainment. The characteristics of the boundary layer (thickness, turbulence intensity) as it encounters the jet will have a significant influence on the entrainment. The Coanda jet attachment was surprisingly easy to obtain, but the effects of curvature on the attached jet and jet–boundary layer interface are only weakly modeled in this study. As the results below will suggest and numerous studies by others have shown, improved turbulence models are the key to this problem. Even so, the relatively simple algebraic turbulence model used here with its low order correction does an adequate job.

Turbulence modeling of the airfoil and Coanda surface was accomplished by modifying a zero equation model developed by Baldwin and Lomax[9] to account for the effect of streamwise streamline curvature on the eddy viscosity. Bradshaw[10] and others have reported on the large effect of streamline curvature in the plane of the mean shear on the turbulence quantities. These effects are often much larger (in some cases as much as an order of magnitude larger) than predicted by dimensional arguments. Bradshaw (1973) suggests modifying the apparent mixing length using a correction analogous to

the Monin-Obouhkov formula for buoyant flows

$$\frac{\ell}{\ell_0} = 1 + \beta \frac{2U/R}{\partial U/\partial y} \tag{7}$$

where $R$ will be the streamline radius of curvature and $\beta$ is an empirical constant on the order of 10. For this investigation a different correction formula, suggested by Baldwin (private communication), was used. This correction is derived from Prandtl's turbulent kinetic energy equation with a curvature suppression term, $F_c$, suggested by Baldwin, Chigier, and Sheaffer[11] in 1973 for a $k-\epsilon$ model. In the notation of Rodi[12], the steady kinetic energy equation with the curvature suppresion term suggestion by Baldwin, et.al[11] is written as

$$U_i \frac{\partial k}{\partial x_i} = \frac{\partial}{\partial x_i}\left(\frac{\nu_t}{\sigma_k}\frac{\partial k}{\partial x_i}\right) + \nu_t\left(\frac{\partial U_i}{\partial x_j} + \frac{\partial U_j}{\partial x_i}\right)\frac{\partial U_i}{\partial x_j} - \epsilon + F_c \tag{8}$$

$$F_c = \left[C_c (U_i U_i)^{\frac{1}{2}}\left(\frac{\partial U_i}{\partial x_j} + \frac{\partial U_j}{\partial x_i}\right)\ell\sqrt{2k}\right]/R \tag{9a}$$

and

$$\nu_t = c_\mu \frac{k^2}{\epsilon}, \quad \epsilon = \frac{c_\mu^{\frac{3}{4}} k^{\frac{3}{2}}}{\ell}, \quad c_\mu \approx .09 \tag{9b}$$

(Note that the $c_\mu$ as used here differs from the $C_\mu$ defined in Eq. (4).) For the high Reynolds number flow under consideration, only stress terms in the normal direction are retained. In addition, convection and diffusion processes are neglected. Under these assumptions the energy equation reduces to

$$\nu_t \omega^2 = \epsilon - \frac{C_c U \omega \ell \sqrt{2k}}{R} \tag{10}$$

This equation can then be solved for $k$ and an expression for $\nu_t$ obtained.

$$\nu_t^2 = c_\mu^{\frac{1}{2}} k \ell^2 = \ell^4 \omega^2 - \frac{C_c U \omega \ell^4 \sqrt{2}}{c_\mu^{\frac{1}{4}} R} \approx \nu_{t_0}^2 - \frac{C_c U \omega \ell^4 \sqrt{2}}{c_\mu^{\frac{1}{4}} R} \tag{11}$$

In this equation $\nu_{t_0}$ is the eddy viscosity computed in the standard Baldwin-Lomax model and $\ell$ is a length scale such that

$$\ell = \begin{cases} \kappa \mathcal{D}(y) y, & \text{if } y \le y_{crossover}\ ; \\ \kappa \mathcal{D}(y_{crossover}) y_{crossover}, & \text{otherwise.} \end{cases} \tag{12}$$

where $y_{crossover}$ is the match point of the inner and outer layers, $\kappa$ is the Karman constant and $\mathcal{D}$ is the usual VanDriest damping function for wall bounded flows.

The only constant to be determined at this point is $C_c$. The calibration of this constant based on other algebraic curvature models (e.g. Ref. 10 and 13) documented in the literature is not straightforward . The constant $C_c$ in Ref. 11 was chosen to be unity, but this choice appears to have been somewhat arbitrary. A calibration of $C_c$ from the $\beta$ in Bradshaw's formula can not be done, as we see it, because of the different behavior of these models except for very small $y^+$ values where curvature is not important. Comparison with other Bradshaw like models proved equally unsatifactory and therfore a numerical calibration of $C_c$ based on the experimental data was performed in the calculations presented below.

## VII. RESULTS

The computational code (ARC2D) has been validated for a wide variety of cases, see Pulliam[1] and Barth, Pulliam, and Buning[14] for numerous examples. The code with the modification for the spiral integration was first validated against a nonspiral standard code for no jet blowing and showed excellent agreement. A conventional 'O' mesh with a closed slot was compared with a spiral mesh solution at $M_\infty = 0.3$ and $\alpha = -5.0°$. Pressure distributions for both computations are compared in Fig. 5. All other measures of accuracy show good to excellent agreement.

Computations for the two Coanda shapes were performed at two Mach numbers, $M_\infty = 0.3$ and $M_\infty = 0.6$. Abramson and Rogers[1] provided the experimental conditions and data. Significant angle of attack corrections for wind tunnel wall interference were suggested to us. An angle of attack correction of $-1.5 \times C_l$ was calibrated by the experimenters. A set of potential code results was used where lifts were matched to the experimental data and circulation was modified using angle of attack changes until the mid-chord pressure gap and leading edge pressure matched experimental values. A calibration across the experimental data produced the factor of $-1.5$. The computations presented here are for an experimental geometric angle of attack $\alpha_{geo} = 0°$ with angle of attack corrections $-1.5C_l$ where $C_l$ is taken from the experimental data. Note that this can be a substantial correction factor since lift levels reach values of $C_l > 2.0$.

Tables 1-4 list the computed cases showing the Coanda type used, Mach number, pressure ratio $P_r$, angle of attack, experimental $C_\mu$, $C_l$, and computed $C_\mu$,$C_l$. The column labeled 'Point' refers to the experimental designation which will be used here to delineate cases.

Plots of $C_l$ against $C_\mu$ for the above cases are shown in Fig. 6 and 7. The computations are able to predict the lift augmentation (lift-slope curves) quite well. In particular, the differences due to changes in Coanda geometry are predicted. For the RE geometry the $M_\infty = 0.3$ produces higher lift augmentation than the $M_\infty = 0.6$ case. For the DE geometry the $M_\infty = 0.6$ case produces more lift augmentation than the $M_\infty = 0.3$.

As can be seen the lift coefficients compare quite well over a broad range of blowing

rates. In order to obtain such good comparisons the turbulence model parameter $C_c$ had to be adjusted. As mentioned above better turbulence modeling is crucial to this problem. Within the constraints of the simple curvature correction used here each case was calibrated by adjusting $C_c$. Specifically, we choose one point from each of the above Tables (Points 38, 304, 733, and 748) and adjusted $C_c$ until the lifts matched the experimental data to within 3%. Once a value of $C_c$ was obtained for one point, all other cases in the associated table were generated with that value. The values of $C_c$ used are listed with the above tables.

The significance of these variations in $C_c$ can only be speculated on. The effect of curvature on the jet–boundary layer interaction and jet–Coanda flowfield are not properly understood but are obviously important. Differences in upper surface boundary layer caused by differences in free stream Mach number and the differences in curvature due to the two Coanda geometries can account for the sensitivity to the curvature correction.

There seems to be a rather large discrepancy for the low Mach number ($M_\infty = 0.3$) nonblowing cases, Points 33 and 728, which occurs for both geometries. The computations simply do not produce the large level of lift obtained in the experiments. The basic airfoil section has about 1% camber which can account for the experimental lift. There may be laminar-turbulent transition effects which the computation cannot account for, or the angle of attack correction scheme may not be applicable for these cases. At the higher Mach number ($M_\infty = 0.6$) the experimental lift is essentially zero and the computations agree better with the experimental data.

Pressure distributions compared with the experimental data for selected cases are shown in Figs. 8-11. In Fig. 8, results are shown for the RE airfoil at $M_\infty = 0.3$, $\alpha_{geo} = 0^\circ$ and a Reynolds number $Re = 3.0 \times 10^6$ for various pressure ratios $P_r$. The key points to look for are comparison of leading edge pressure distribution and midchord pressure gap which indicate that the angle of attack correction is proper and the blowing rate (mass flow $C_\mu$) is good. Note that since angle of attack corrections are needed and the mass flow out the jet has a strong influence on the solution, there is the possibility of predicting lifts that match experimental data for a wide variety of angles and mass flow rates. In the results shown here the leading edge pressure and midchord pressure match quite well at least up until the higher pressure ratio case. As shown in Table 1 lift coefficient is predicted accurately for these cases.

The pressure distributions in the regions before the jet–Coanda interaction on the upper and lower surface are important indicators of having a good prediction of the incoming boundary layers which stongly influence the entrainment mechanism. The results shown in Fig. 8 show fairly good pressure gradients in those regions.

Plates 3a and 3b show Mach contours in color for results from Point 33. The color contour range was taken between the minimum and maximum Mach number with blue being $M = 0.0$ and magenta $M = 0.36$. Note the continuity of Mach contours throughout the flow field even across wrap boundaries, as expected because

of the spiral integration discussed above. This a case with no jet blowing and we obtain the massive base flow separation. Plate 3b shows the extent of the separation region and gives an indication of the boundary layers on the upper and lower surfaces. Plates 4a and 4b show Mach contours for Point 38 and have the color scale blue for $M = 0.0$ to magenta for $M = 1.1$. The jet remains attached to the Coanda surface (the Coanda effect) which produces a region where the jet–upper surface boundary layer can interact. The shear layer between the jet and the upper surface flow produces an entrainment of fluid, i.e. a transfer of high momentum from the jet to the lower momentum upper surface boundary layer flow. It is easily seen from a comparison with Plate 3 that stagnation points have moved below the leading and trailing edges indicating increased circulation. The base flow separation has been moved to the lower part of the Coanda and reduced. The wake–shear layer region where the jet detaches from the Coanda surface is deflected.

Figure 9 shows pressure distributions for some of the $M_\infty = 0.6$, $\alpha_{geo} = 0°$, and $Re = 5.0 \times 10^6$ RE cases. The leading edge, midchord pressure gap and lifts are in good agreement with the experimental data. The trailing edge pressure gradients appear to be good but the absolute level of the pressure in those regions is a little low. Even so the results are quite good overall. In this case the jet detaches from the Coanda surface sooner than for the lower Mach number case because of the lower mass flow rate. There is less overall entrainment and therefore less lift augmentation. The separation region is more like a base flow separation.

Pressure distributions for the DE Coanda are shown in Fig. 10 ($M_\infty = 0.3$, $\alpha_{geo} = 0°$ and $Re = 2.88 \times 10^6$) and Fig. 11 ($M_\infty = 0.6$, $Re = 5.0 \times 10^6$). The quality of the results is similar to the RE solutions. The leading edge pressure, midchord pressure gaps and pressure gradients again compare quite well with the experimental data. For the DE, the jet detaches from the Coanda surface sooner than in the RE case even though the mass flow rates ($C_\mu = 0.0322$ for the RE and $C_\mu = 0.036$ for the DE) are similar. This is a direct response to the Coanda surface geometry (curvature) since both cases use the same forebody, incoming Mach number and geometric of attack. Note that since different lift levels were reached in the experiment different angle of attack corrections were needed in the computations.

In Plate 5 we show Mach color contours for four of the cases. Plate 5a is for RE Point 38, Plate 5b for RE Point 304, Plate 5c for DE Point 733 and Plate 5d for DE point 748. These are Mach contour maps where each region is colored based on the local Mach number. Contour lines are added to enhance levels. The Plates give a comparative picture of the structure of the flow fields. One can note the entrainment of the upper surface flow into the jet wake flow, the deflections of the wake centerlines and the relative lengths of the jets, detachment points, and separation regions.

## VI SUMMARY

A computational capability for computing Navier-Stokes solutions for circulation controlled airfoils has been developed. The spiral grid topology allows us to integrate

the jet plenum chamber and exterior flow as a single unit. The cases presented here are representative of the computational capability. The results compare quite well with experiment, predicting pressure distributions, lift levels, lift augmentation, Coanda geometry effects, and flow field structure for a wide variety of blowing rates and two Mach numbers. The results are not completely predictive since the turbulence model had to be calibrated for a curvature correction. It is obvious that better turbulence modeling is needed for this problem. Future work will concentrate on the turbulence modeling and attempting to compute stall boundaries and understand the physics of the stall and general flow field.

## VI ACKNOWLEDGEMENTS

The authors would like to thank Drs. J. Abramson and E. Rogers of David W. Taylor Naval Ship Research and Development Center for supplying the experimental data and for many helpful discussions on the experiments and in evaluating the computations. We also thank Dr. N Wood of Stanford for similar discussions and invaluable suggestions. Thanks to Dr. B. Baldwin for help with the turbulence modeling and Dr. P. Buning for help with the graphics and useful discussions on the physics of the computed flows.

| Table 1. RE Coanda $M_\infty = 0.3$, $\alpha_{geo} = 0.0°$, $C_c = 1.6$ | | | | | | |
|---|---|---|---|---|---|---|
| Point | $P_r$ | $\alpha$ | $C_\mu$ Exp. | $C_l$ Exp. | $C_\mu$ Comp. | $C_l$ Comp. |
| 33 | 1.000 | -0.11 | 0.0000 | 0.169 | 0.0000 | 0.055 |
| 35 | 1.137 | -0.93 | 0.0094 | 0.616 | 0.0089 | 0.606 |
| 36 | 1.284 | -1.66 | 0.0179 | 1.106 | 0.0176 | 1.127 |
| 37 | 1.432 | -2.18 | 0.0253 | 1.454 | 0.0259 | 1.496 |
| 38 | 1.573 | -2.65 | 0.0322 | 1.764 | 0.0322 | 1.743 |
| 39 | 1.705 | -3.00 | 0.0376 | 2.000 | 0.0388 | 2.073 |

| Table 2. RE Coanda $M_\infty = 0.6$, $\alpha_{geo} = 0.0°$, $C_c = 4.4$ | | | | | | |
|---|---|---|---|---|---|---|
| Point | $P_r$ | $\alpha$ | $C_\mu$ Exp. | $C_l$ Exp. | $C_\mu$ Comp. | $C_l$ Comp. |
| 301 | 1.000 | 00.00 | 0.0000 | 0.036 | 0.0000 | 0.033 |
| 302 | 1.202 | -0.29 | 0.0032 | 0.191 | 0.0029 | 0.106 |
| 304 | 1.533 | -0.58 | 0.0075 | 0.388 | 0.0074 | 0.375 |
| 305 | 1.701 | -0.71 | 0.0094 | 0.472 | 0.0094 | 0.472 |
| 307 | 2.045 | -0.95 | 0.0132 | 0.634 | 0.0134 | 0.695 |

| Table 3. DE Coanda $M_\infty = 0.3$, $\alpha_{geo} = 0.0°$, $C_c = 2.0$ | | | | | | |
|---|---|---|---|---|---|---|
| Point | $P_r$ | $\alpha$ | $C_\mu$ Exp. | $C_l$ Exp. | $C_\mu$ Comp. | $C_l$ Comp. |
| 728 | 1.000 | -0.25 | 0.0000 | 0.167 | 0.0000 | 0.033 |
| 729 | 1.068 | -0.42 | 0.0041 | 0.281 | 0.0041 | 0.229 |
| 731 | 1.300 | -1.06 | 0.0176 | 0.705 | 0.0182 | 0.745 |
| 732 | 1.488 | -1.40 | 0.0252 | 0.932 | 0.0258 | 0.957 |
| 733 | 1.588 | -1.79 | 0.0322 | 1.192 | 0.0326 | 1.202 |
| 734 | 1.716 | -2.05 | 0.0377 | 1.367 | 0.0385 | 1.411 |
| 735 | 1.188 | -2.31 | 0.0445 | 1.541 | 0.0461 | 1.550 |

| Table 4. DE Coanda $M_\infty = 0.6$, $\alpha_{geo} = 0.0°$, $C_c = 2.2$ | | | | | | |
|---|---|---|---|---|---|---|
| Point | $P_r$ | $\alpha$ | $C_\mu$ Exp. | $C_l$ Exp. | $C_\mu$ Comp. | $C_l$ Comp. |
| 744 | 1.000 | -0.11 | 0.0000 | 0.073 | 0.0000 | 0.048 |
| 745 | 1.168 | -0.36 | 0.0026 | 0.237 | 0.0024 | 0.135 |
| 747 | 1.526 | -0.78 | 0.0074 | 0.518 | 0.0074 | 0.513 |
| 748 | 1.709 | -0.96 | 0.0095 | 0.614 | 0.0096 | 0.627 |
| 751 | 2.038 | -1.21 | 0.0130 | 0.805 | 0.0133 | 0.806 |

## REFERENCES


1. Abramson, J., and Rogers, E., *High Speed Characteristics of Circulation Control Airfoils*, AIAA Paper 83-0265 (1983).
2. Wood, N. and Nielsen, J., *Circulation Control Airfoils Past, Present, Future*, AIAA Paper 85-0204 (1985).
3. Pulliam, T. H., *Euler and Thin Layer Navier-Stokes Codes : ARC2D, ARC3D, Notes for Computational Fluid Dynamics User's Workshop*, UTSI E02-4005-023-84, March 1984.
4. Vinokur, M., *On One-Dimensional Stretching Functions for Finite-Difference Calculations*, J. Comp. Phys. (1983), p. 215–234.
5. Steger, J. L., *Implicit Finite Difference Simulation of Flow About Arbitrary Geometries with Application to Airfoils*, AIAA Paper 77-665 (1977).
6. Pulliam, T. H., and Steger, J. L., *Recent Improvements in Efficiency, Accuracy, and Convergence for Implicit Approximate Factorization Algorithms*, AIAA Paper 85-0360 (1985).
7. Pulliam, T. H., *Artificial Dissipation Models for the Euler Equations*, AIAA Paper 85-0438 (1985).
8. Pulliam, T. H., and Chaussee D.S., *A Diagonal Form of an Implicit Approximate Factorization Algorithm*, J. Comp. Phys. **39** (1981), p. 347.
9. Baldwin, B. S., and Lomax, H., *Thin Layer Approximation and Algebraic Model for Separated Turbulent Flows,*, AIAA Paper No. 78-257 (1978).
10. Bradshaw P., *The Effects of Streamline Curvature on Turbulent Flow.*, AGARDograph no. 169. (1973).
11. Baldwin B., Chigier N., and Sheaffer S., *Decay of Far-Flowfield Trailing Vortices.*, AIAA Journal, Vol 11 (1973), p. 1601.
12. Rodi W., *Proceedings of École d'Été d'Analyse Numérique - Modélisation numerique de la Turbulence, Clamart, France.*
13. Shrewsbury, G. D., *Analysis of Circulation Control Airfoils Using An Implicit Navier-Stokes Solver*, AIAA Paper 85-0171 (1985).
14. Barth, T. J., Pulliam, T. H., and Buning, P. G., *Navier Stokes Computations for Exotic Airfoils*, AIAA Paper 85-0109 (1985).

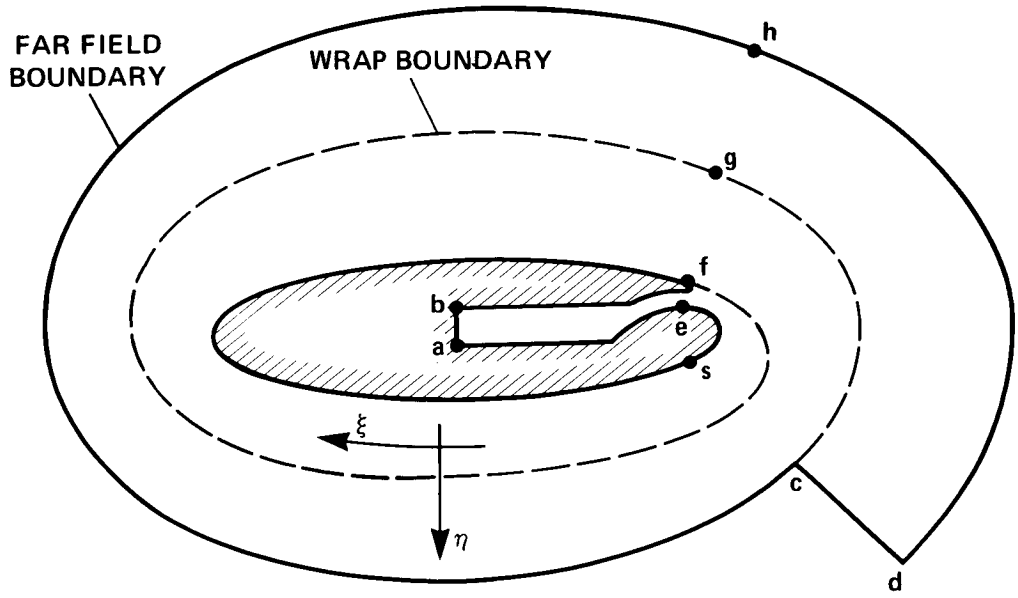


PHYSICAL SPACE

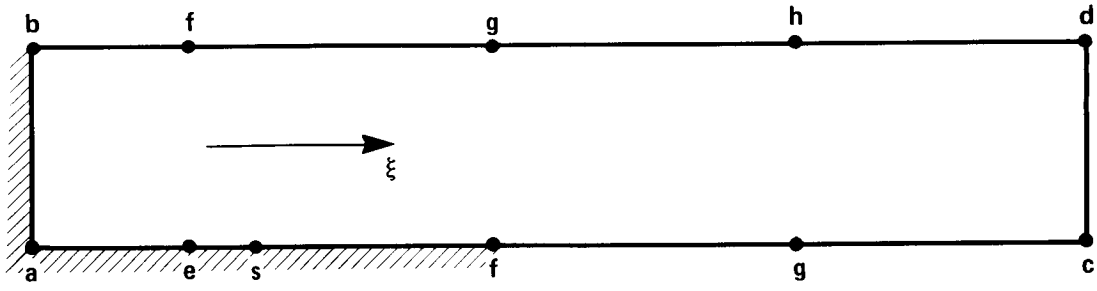


ξ-COMPUTATIONAL SPACE

Figure 1. Computational Mapping For $\xi$ Orientation Topology.

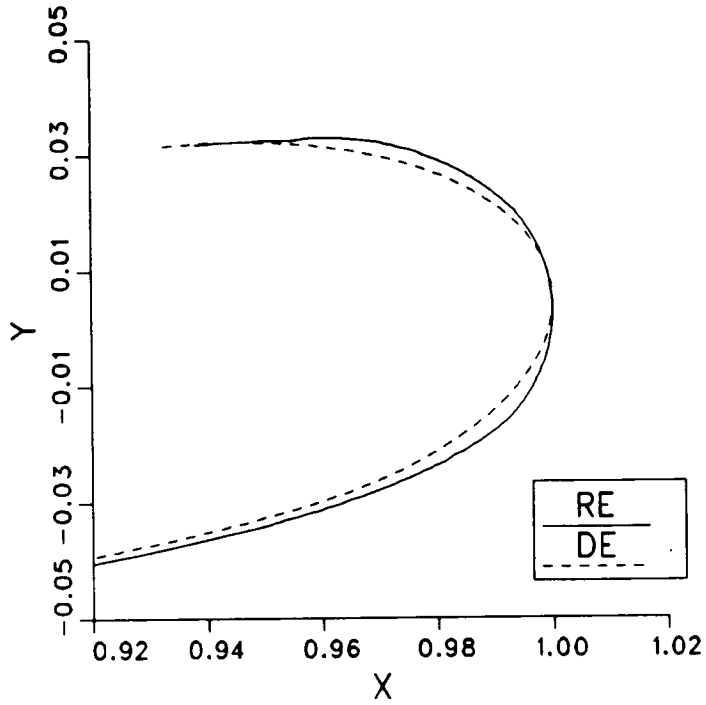


Figure 2. Coanda Geometry For RE and DE Airfoils.

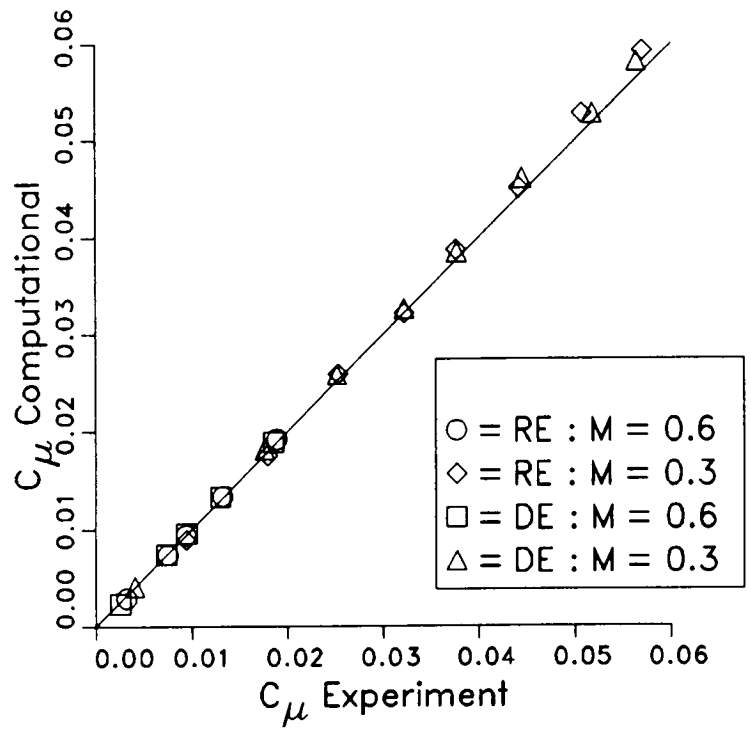


Figure 3. Correlation Between Experimental and Computational Mass Flows. Slot Height = 0.0025, $\alpha_{jet}$ = 0.0.

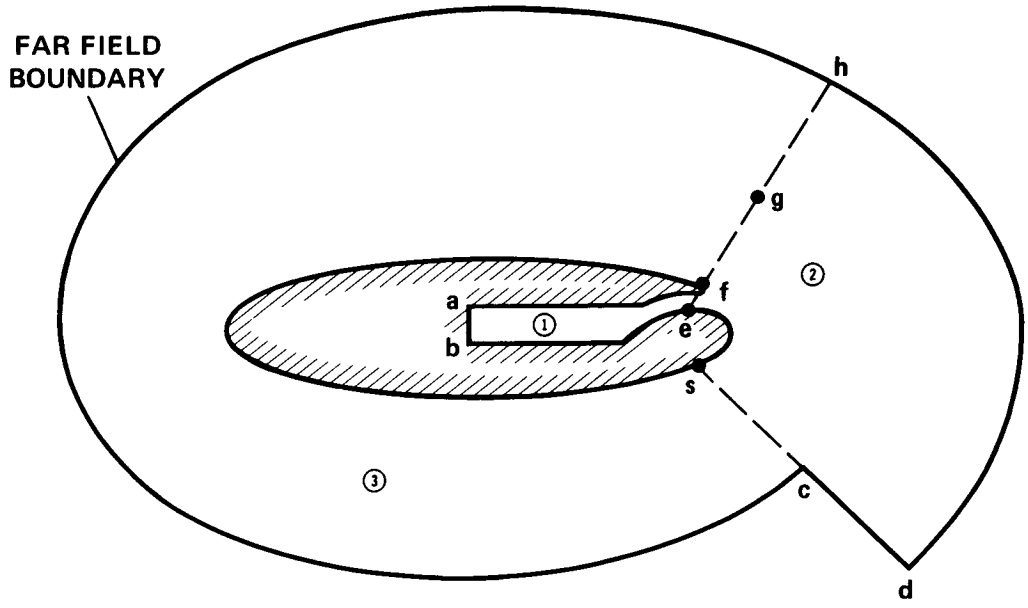


PHYSICAL SPACE

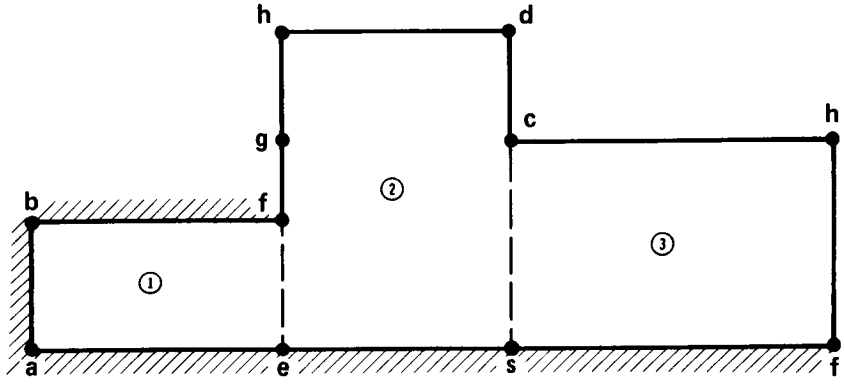


$\eta$-COMPUTATIONAL SPACE

Figure 4. Computational Mapping For $\eta$ Orientation Topology.

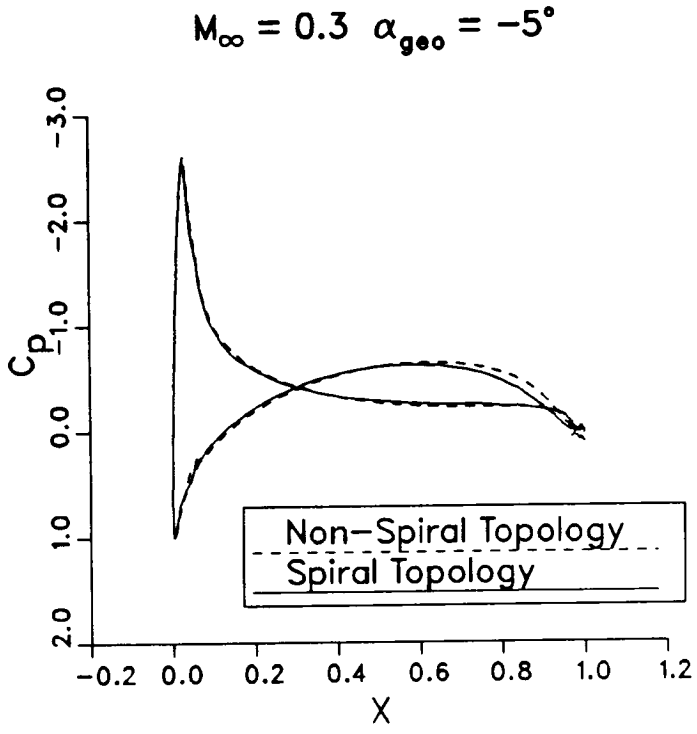


Figure 5. Comparison Between Non-Spiral and Spiral Integrations For A No Blowing Case.

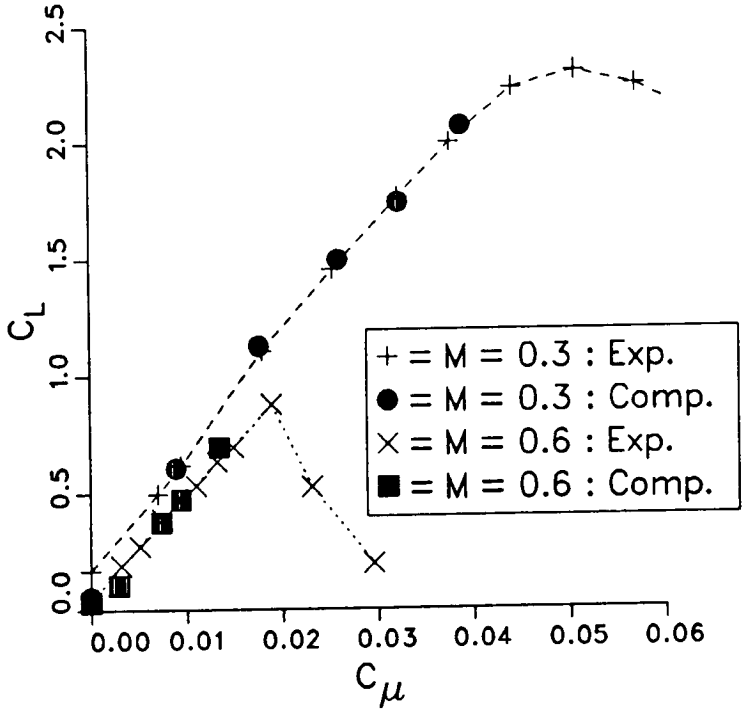


Figure 6. Lift Augmentation Curves For RE Geometry At $\alpha_{geo} = 0.0$.

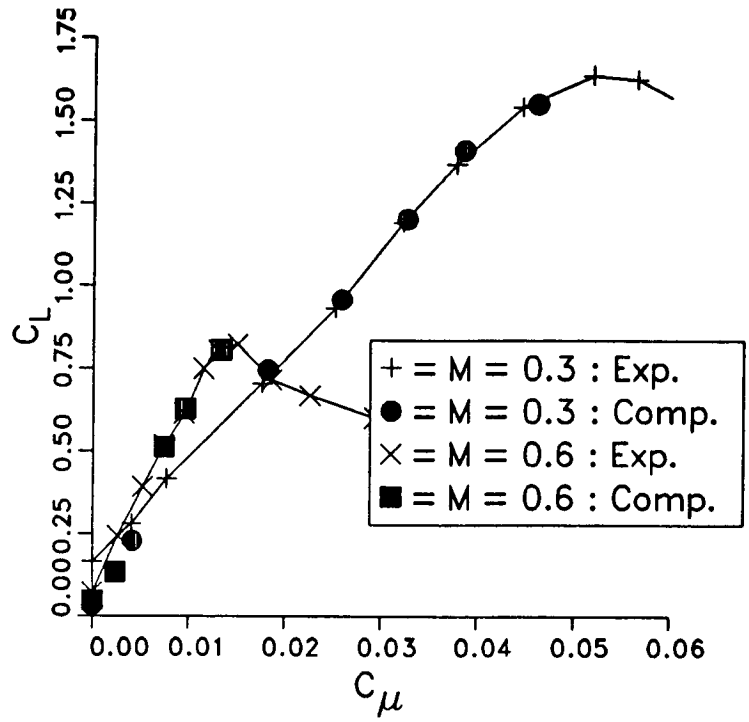


Figure 7. Lift Augmentation Curves For DE Geometry At $\alpha_{geo} = 0.0$.

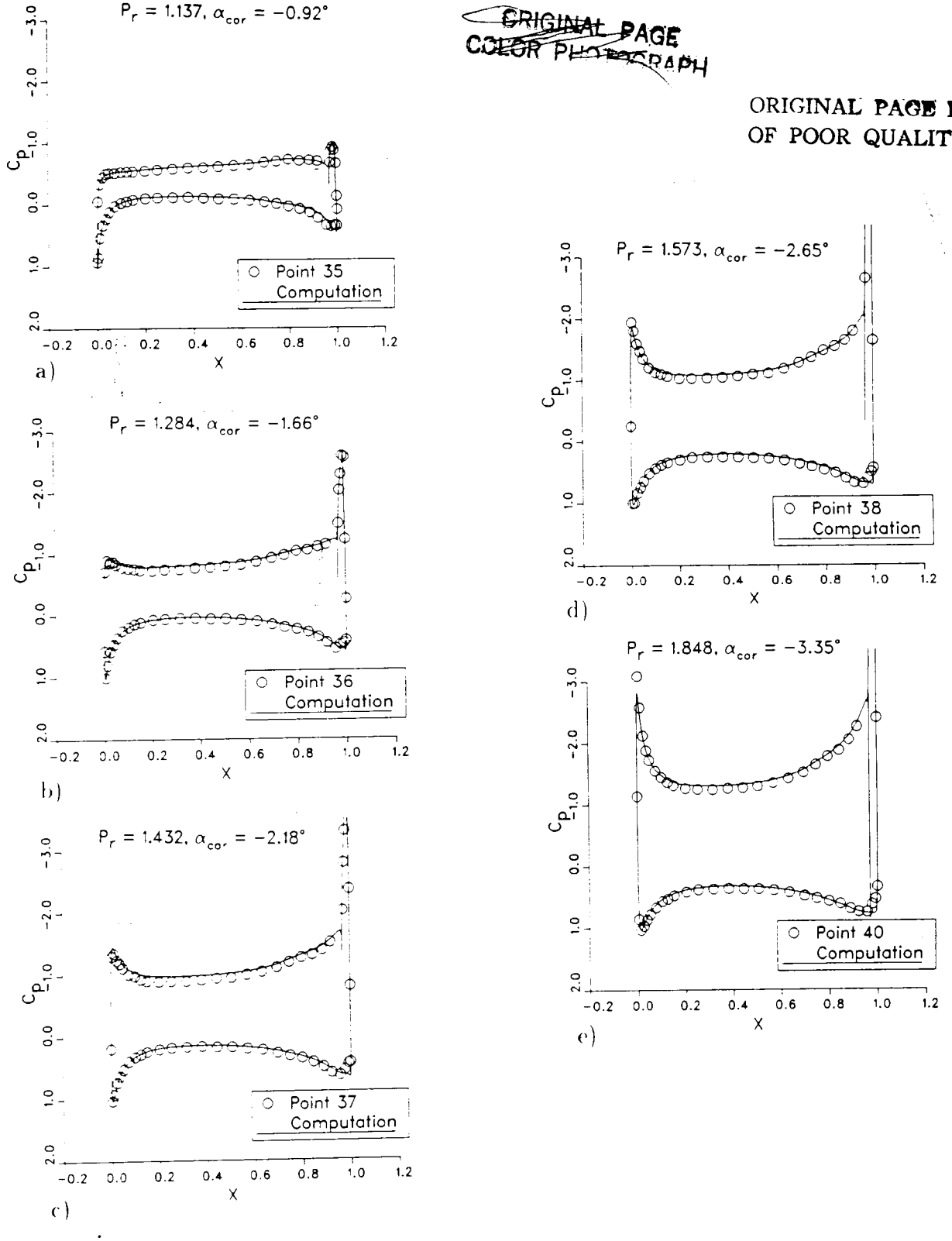


Figure 8. Pressure Distributions For RE Geometry, $M_\infty$ = 0.3, $alpha_{geo}$ 0.0.

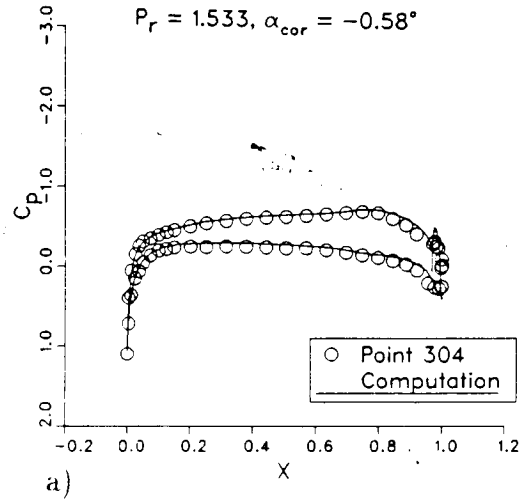


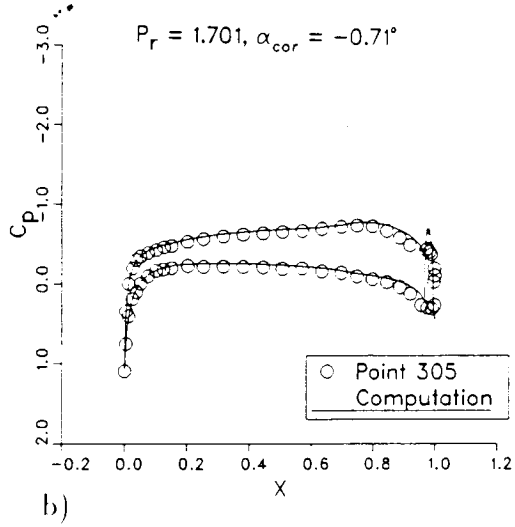


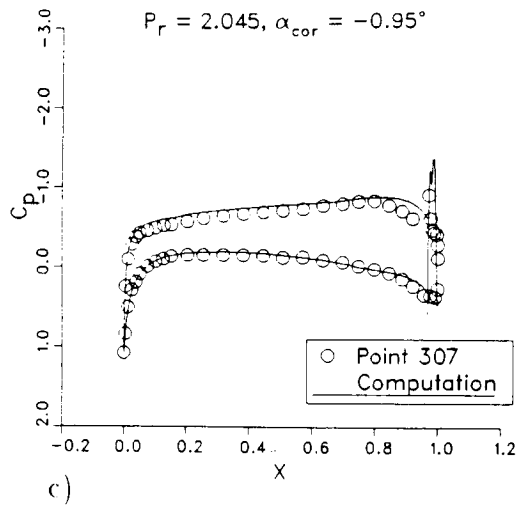


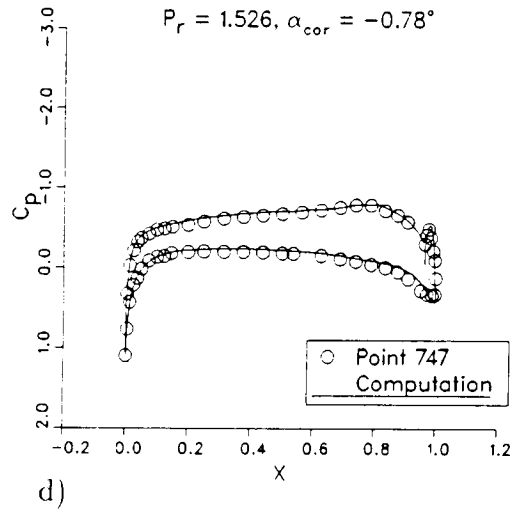


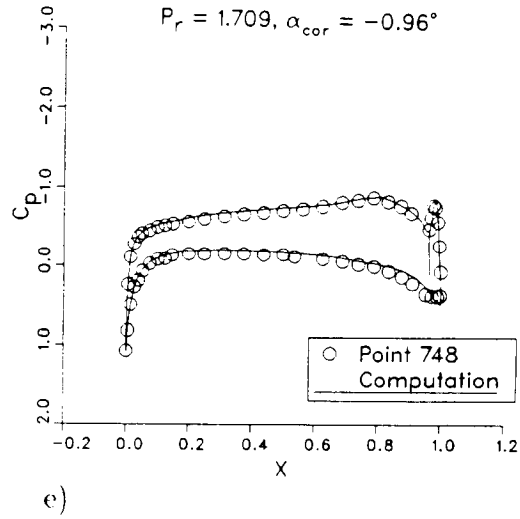




Figure 9. Pressure Distributions For RE Geometry.
$M_\infty$ 0.6, $alpha_{geo}$ 0.0.

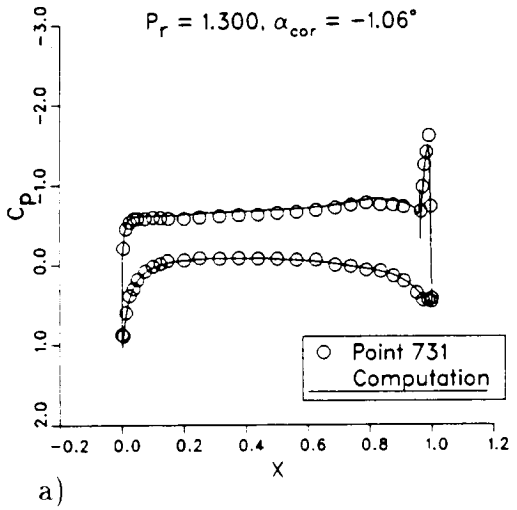


a)

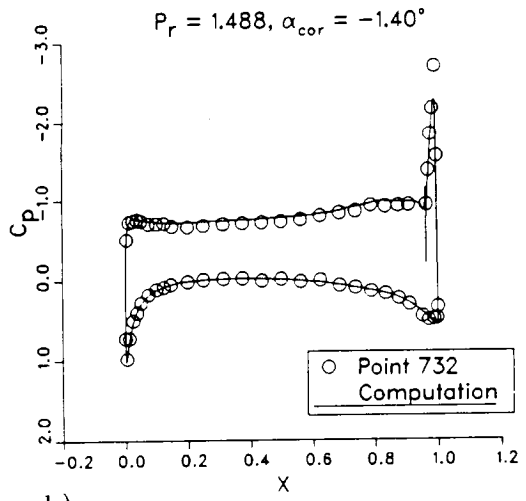


b)

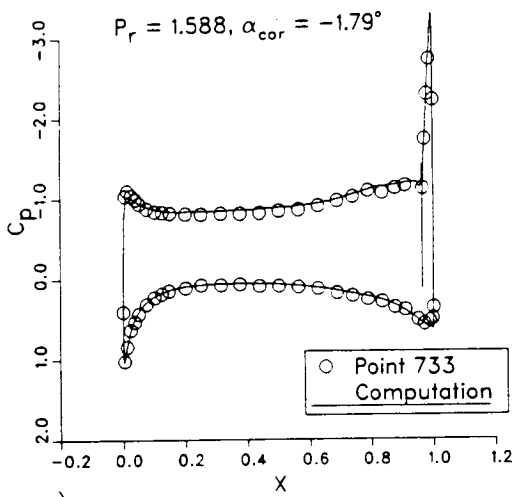


c)

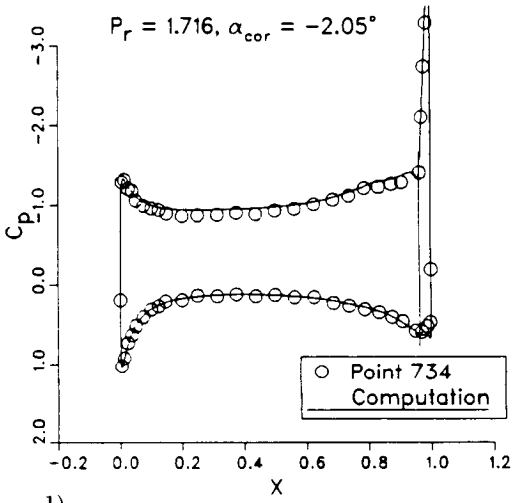


d)

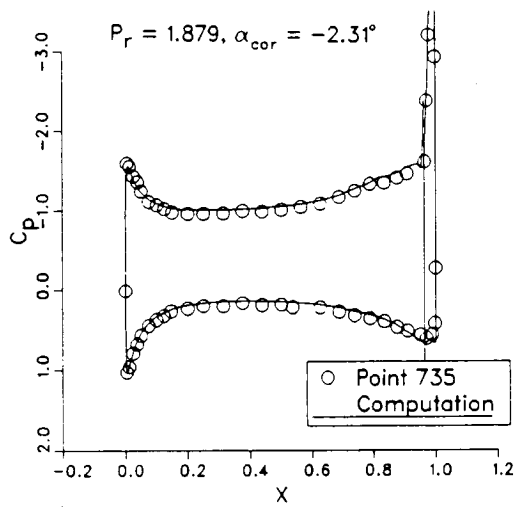


e)

Figure 10. Pressure Distributions For DE Geometry.
$M_\infty$ = 0.3, $alpha_{geo}$ = 0.0.

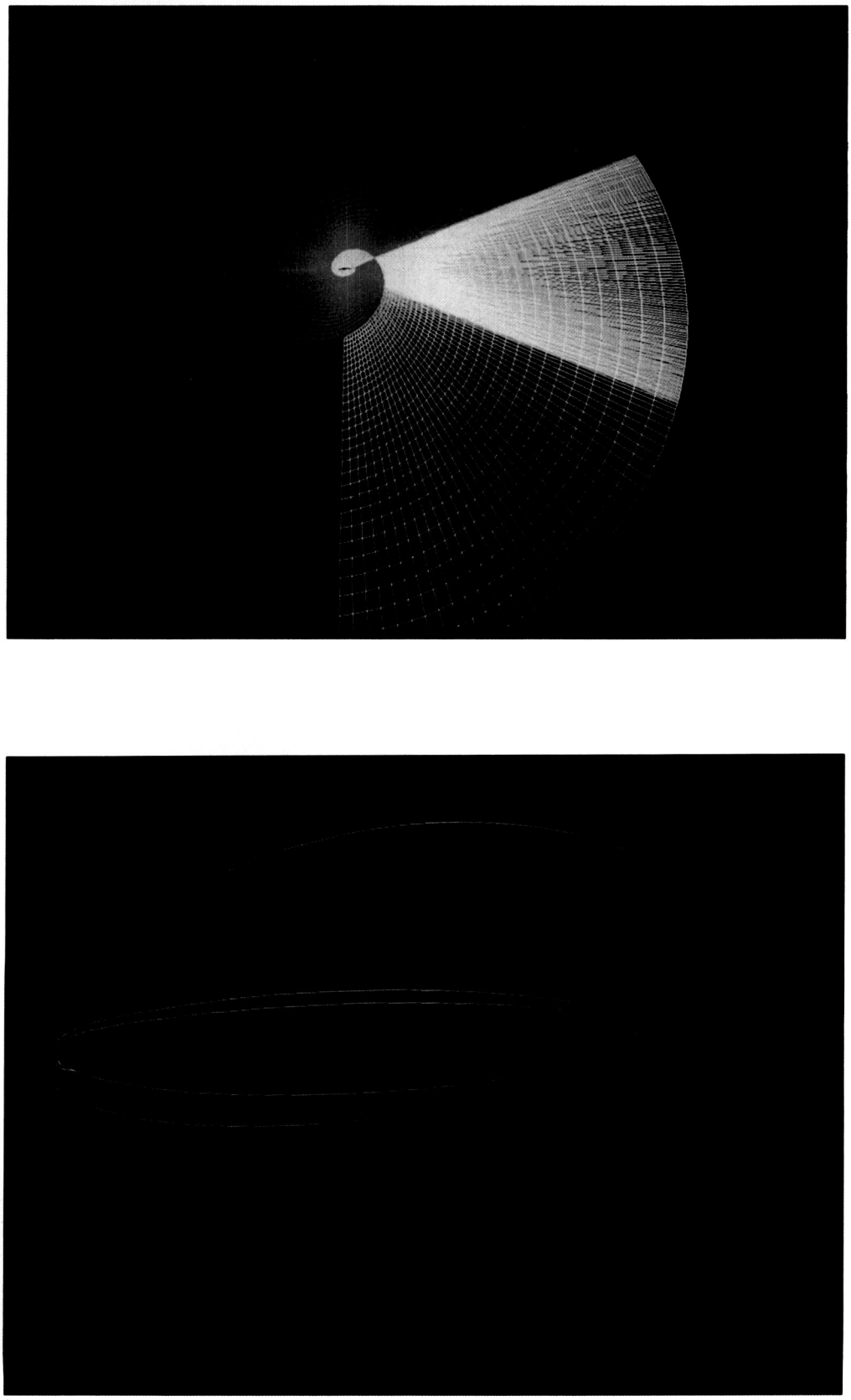

Plate 1. Spiral Grid Topology Used In Computations Showing grid Distributions and Spiral Wrap Boundaries For $\xi$ Orientation.

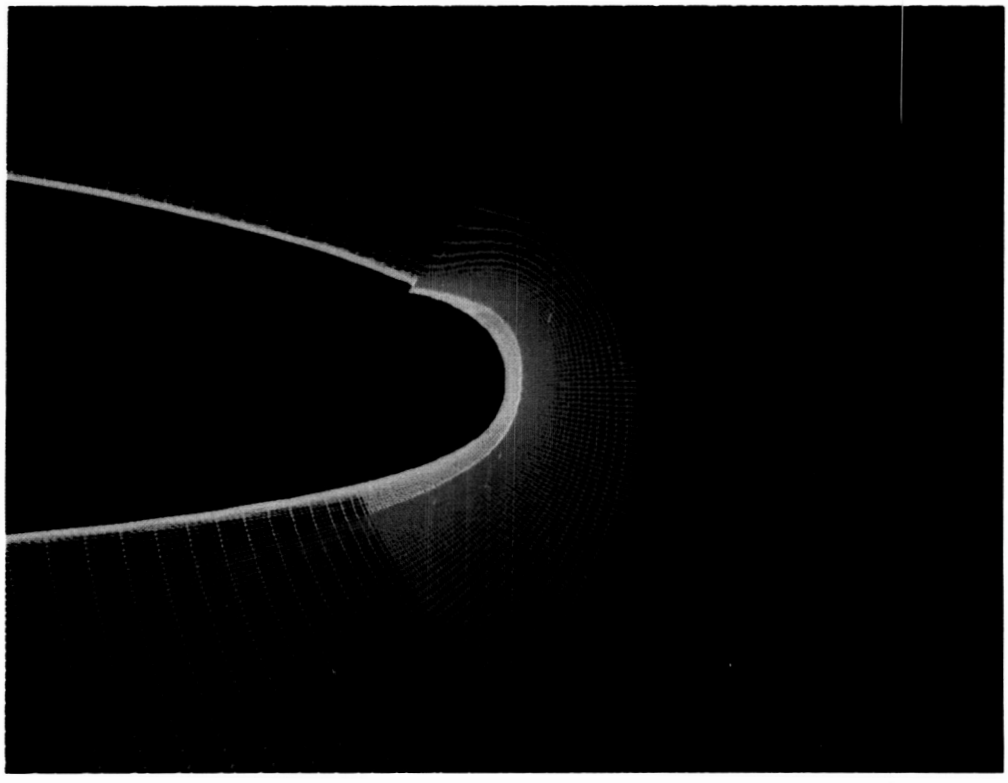

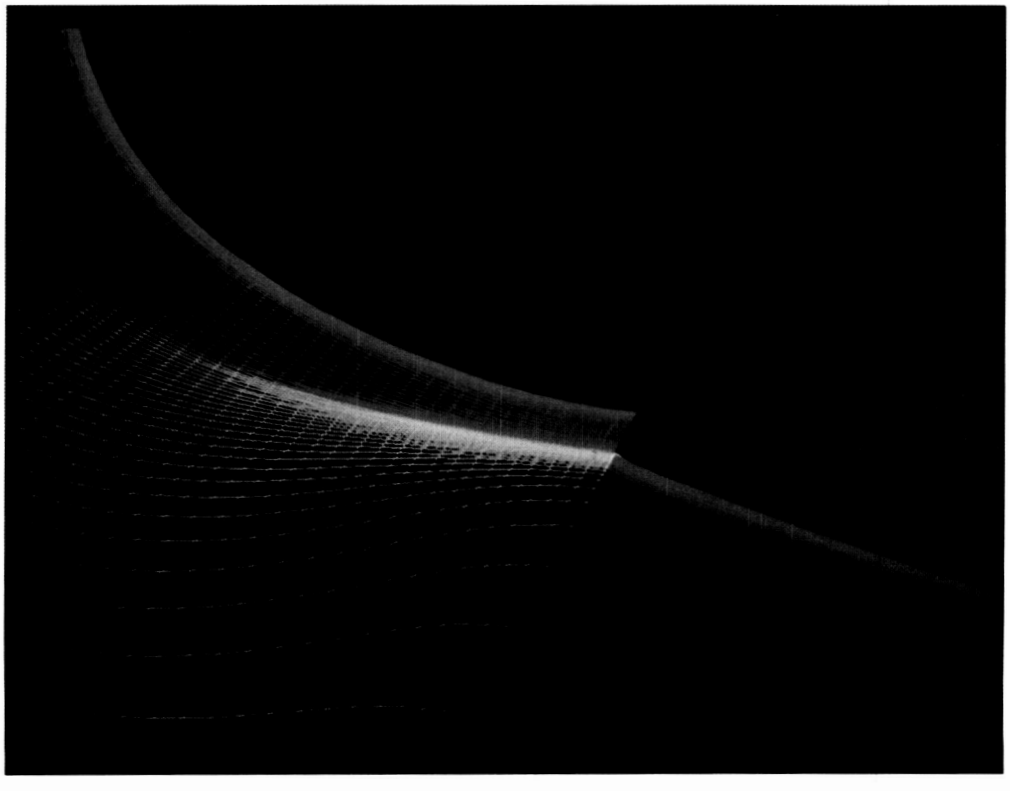

**Plate 1.** Concluded.

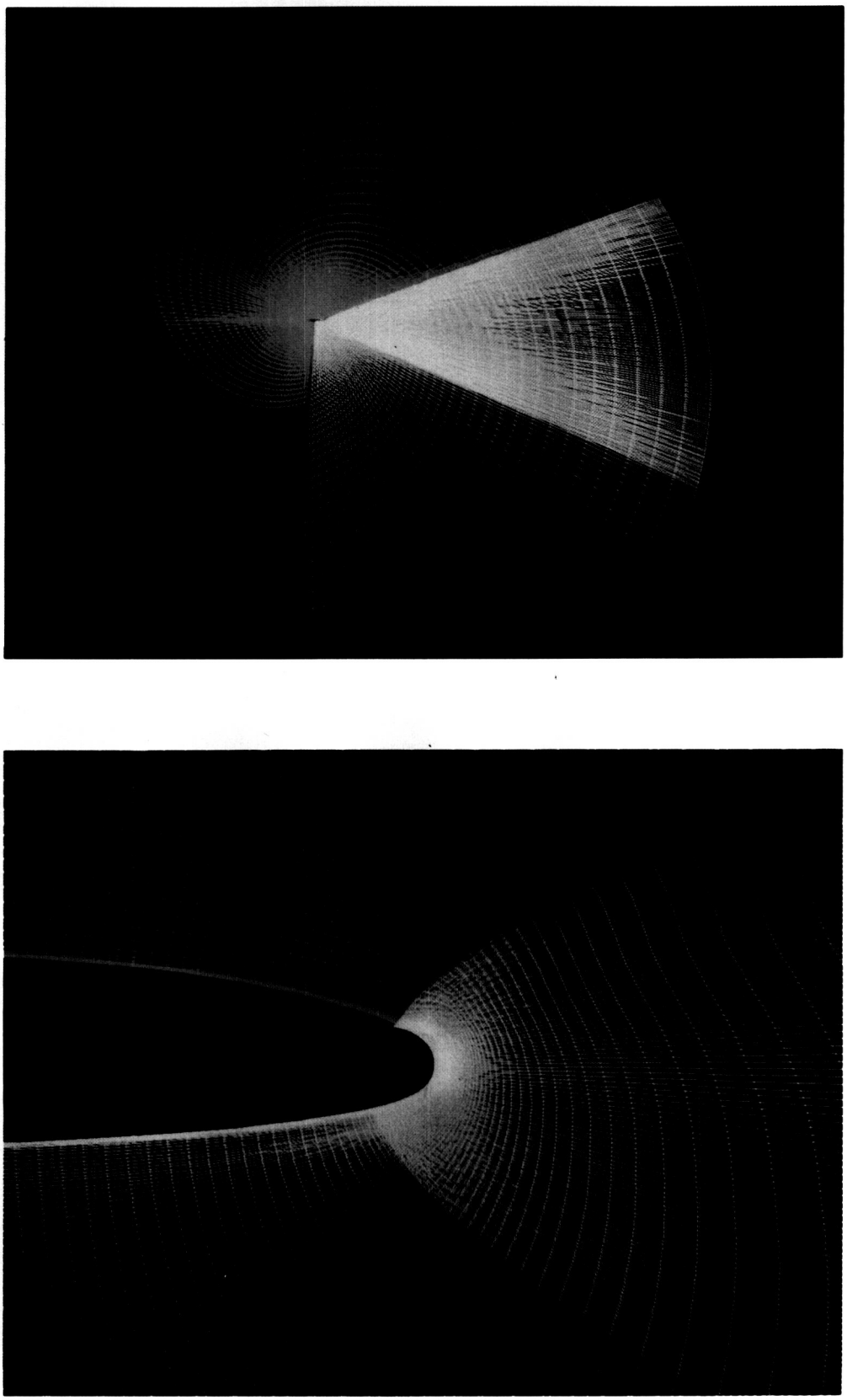

Plate 2. Spiral Grid Topology Used In Computations Showing grid Distributions and Spiral Wrap Boundaries For $\eta$ Orientation.

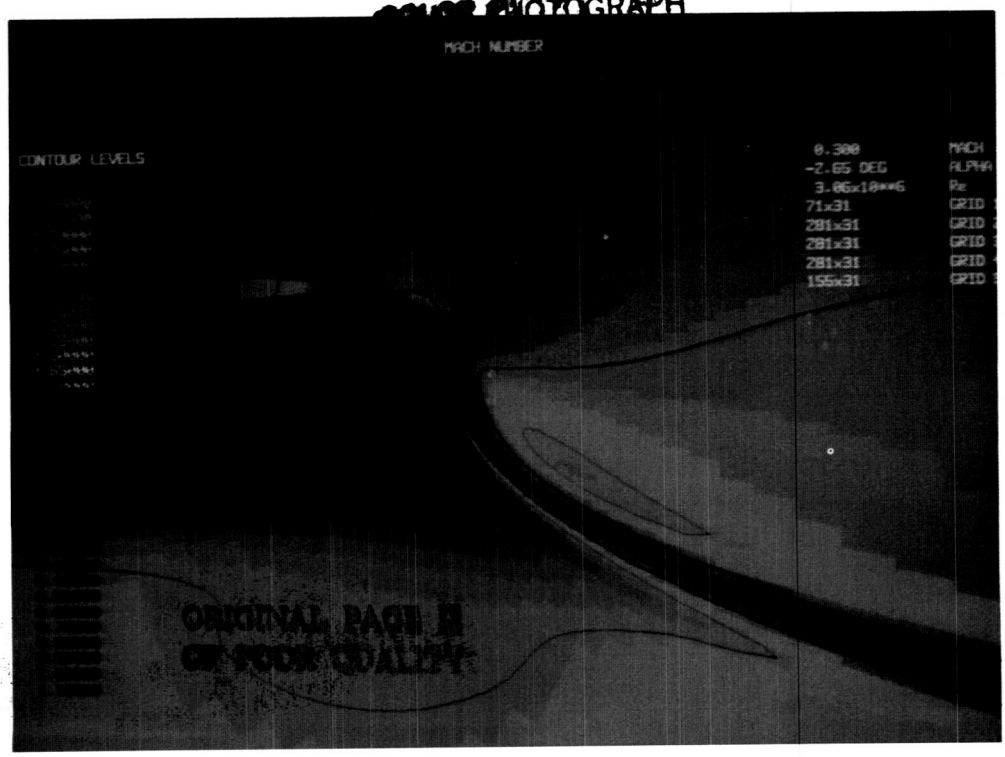


a) Point 38.

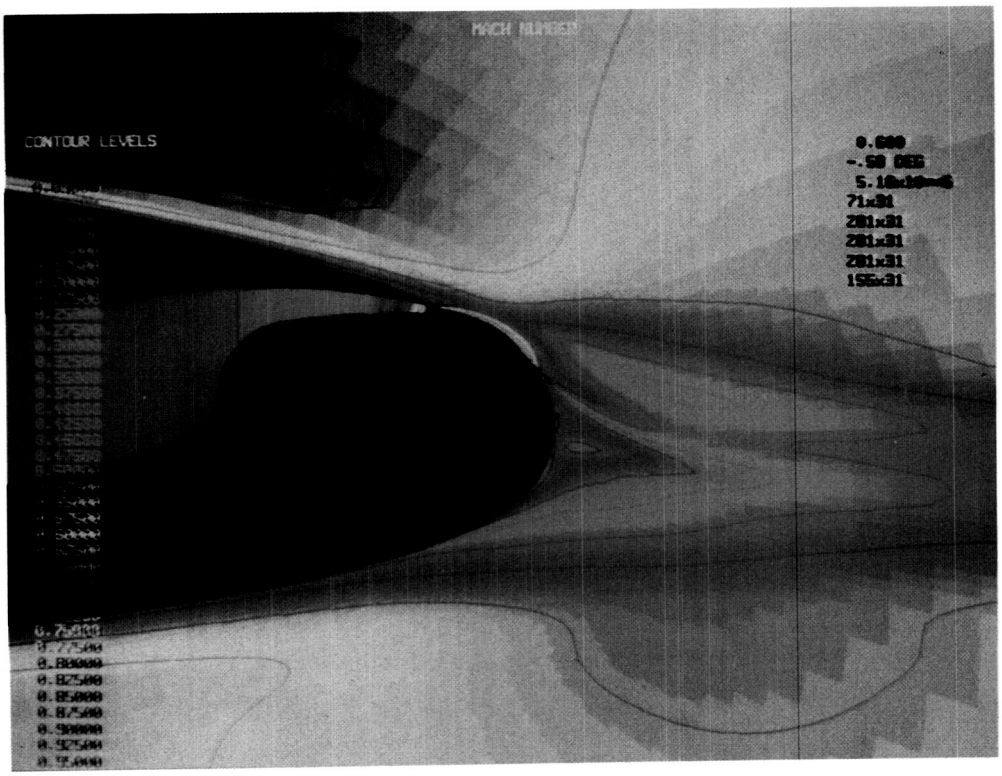


b) Point 304.

Plate 5. Color Mach Contours Showing The Relative Differences In The Flow Structures Due To Mach Number and Coanda Geometry.

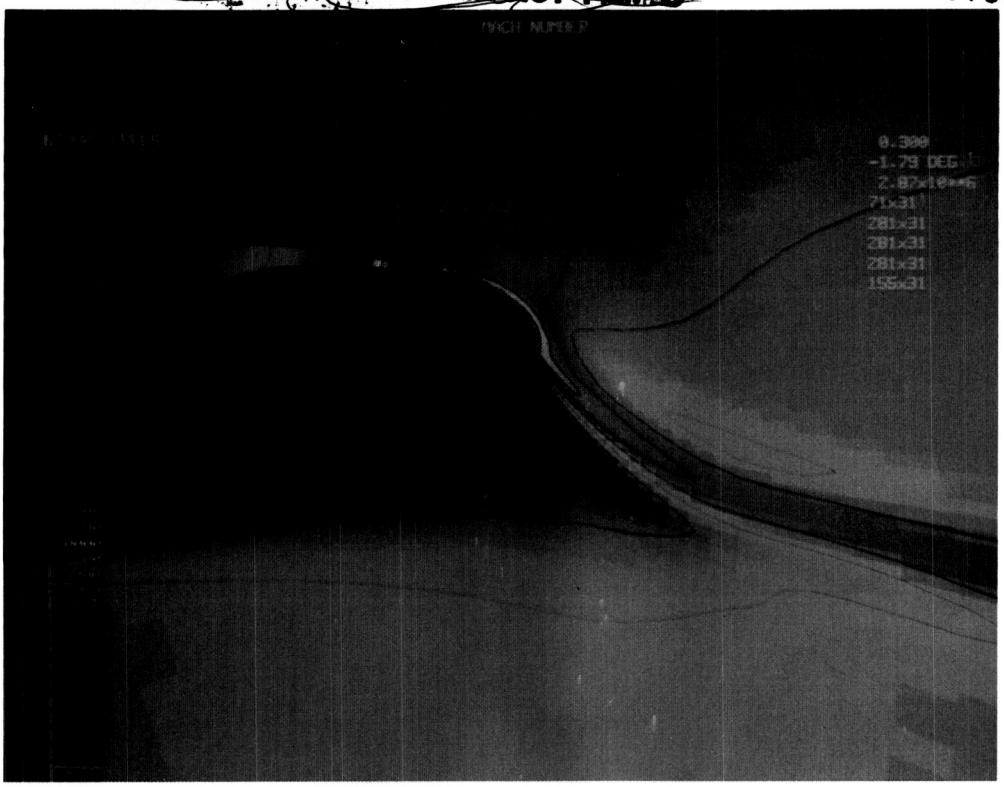


c) Point 733.

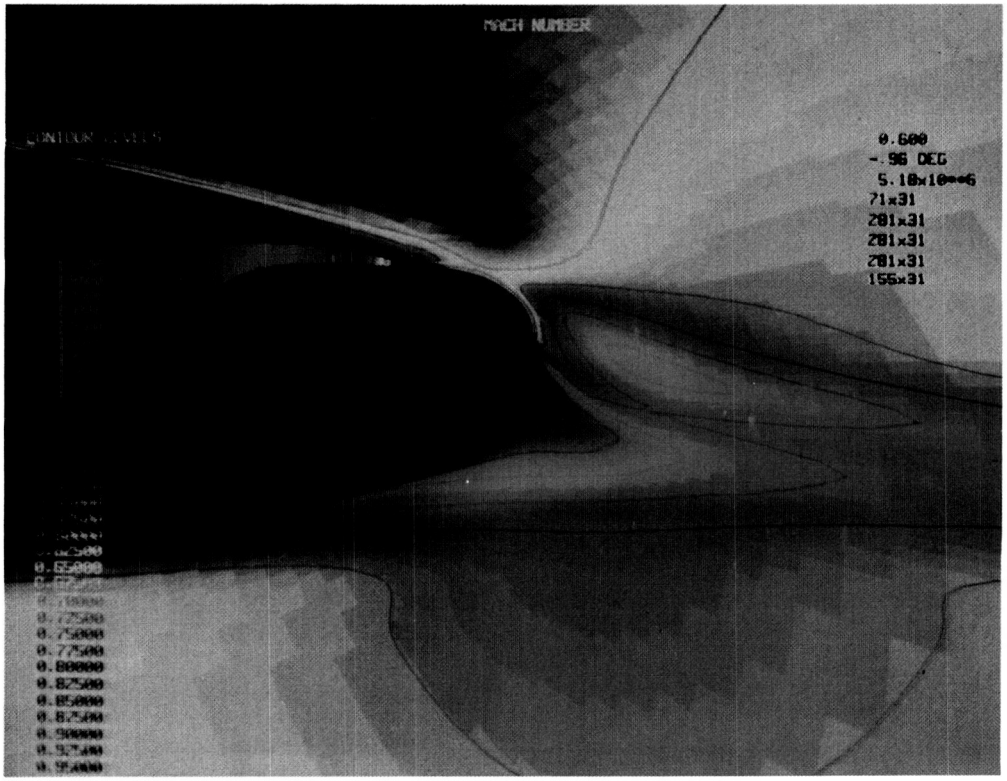


d) Point 748.

Plate 5. Concluded.